Fuel 346 (2023) 128222

Contents lists available at ScienceDirect

Fuel

journal homepage: www.elsevier.com/locate/fuel

Directly irradiated fluidized bed autothermal reactor (DIFBAR): Hydrodynamics, thermal behaviour and preliminary reactive tests

Stefano Padula [a], Maurizio Troiano [a,b], Claudio Tregambi [b,c], Roberto Solimene [b,*], Piero Salatino [a,b]

[a] Dipartimento di Ingegneria Chimica, dei Materiali e della Produzione Industriale, Università degli Studi di Napoli Federico II, Piazzale V. Tecchio 80, 80125 Napoli, Italy
[b] Istituto di Scienze e Tecnologie per l'Energia e la Mobilità Sostenibili (STEMS), Consiglio Nazionale delle Ricerche, Piazzale V. Tecchio 80, 80125 Napoli, Italy
[c] Dipartimento di Ingegneria, Università degli Studi del Sannio, Piazza Roma 21, 82100 Benevento, Italy

ARTICLE INFO

Keywords:
Fluidized beds
Circulating fluidized beds
Thermochemical energy storage
Concentrated solar thermal
Autothermal reactor

ABSTRACT

The advancements of the Concentrating Solar Thermal (CST) technologies in the heat and power sector are pushing researchers to find new ways to exploit solar energy. Solar-driven thermochemical processes can open new scenarios and set a milestone towards a greener industry. This paper presents the development of a Directly Irradiated Fluidized Bed Autothermal Reactor (DIFBAR), that exploits fluidization technology and the principle of an autothermal reactor to carry out solar chemical processes with high efficiency. The viability of recovering the sensible energy of the solid products to preheat the reactants is studied in an experimental prototype that couples a cavity receiver/reactor and a countercurrent double-pipe heat exchanger. The prototype is operated as a circulating fluidized bed: the inner tube of the heat exchanger is a fluidized bed riser, the receiver works as a gas–solid separator, the outer tube (annulus) of the heat exchanger is an overflow standpipe and a buffer tank (reservoir) connects the annulus to the riser, closing the loop. The reservoir can also be operated as a fluidized bed reactor like in a dual-fluidized bed system. The first experimental results are reported using a Geldart B sand as bed inventory. A hydrodynamic study has been carried out to verify proper control of the system. Solid circulation rates have been determined and match the design target of 1.4 g/s. Pressure measurements have been used to control bed levels and the flow of the sand through the standpipe. The effects of gas velocities and outlet pressure drops are reported. Internal gas flow patterns have been determined by a gas tracing technique. Undesired gas by-passing streams are very small and can be zeroed by regulating the operating conditions. High temperature experiments have been conducted with a high-flux solar simulator under inert and reactive conditions, to prove the operating principle of the reactor. Steady state temperature profiles have been analyzed to assess the performance of the heat exchanger: the heat transfer coefficient ranges between 340 and 490 W/(m^2 K). The operability of a solar-driven chemical process has been proved by calcining a batch of magnesium carbonate ($MgCO_3$) particles, added to the inventory.

1. Introduction

Clean and renewable energy technologies are urgently needed to stop global warming and to drive the economic recovery after the Covid-19 crisis and the outbreak of the Russian-Ukrainian conflict. In this frame, solar energy has a great potential to address these issues. Concentrated Solar Thermal (CST) technology is a dawning solution, that uses solar radiation as a heat source, by concentrating solar rays with an array of sun-tracking mirrors (heliostats). A Heat Transfer Fluid (HTF) usually absorbs solar energy and supplies a conventional thermal power plant. Despite high capital costs, CST displays some promising features: simple integration with Thermal Energy Storage (TES) [1], small requirements for critical raw materials [2], and possible hybridization with other renewable energy sources. TES allows to extend the operation of a CST plant after sunset and is fundamental to improve its economic sustainability, allowing to optimize the size of the heliostat field and to produce electricity during peak demand hours. Molten salts mixtures are used today as HTFs and TES media in many pioneering CST

---

* Corresponding author.
E-mail address: roberto.solimene@cnr.it (R. Solimene).

https://doi.org/10.1016/j.fuel.2023.128222
Received 31 December 2022; Received in revised form 6 March 2023; Accepted 23 March 2023

power plants [3]. New solutions are being proposed to reduce storage volumes and increase operative temperatures [4]. One of the major drawbacks of molten salts is the maximum storage temperature (up to 565 °C), that limits the efficiency of the power cycle. The development of particle receivers handling granular solids as HTFs and TES media is of great interest, since they could withstand temperatures of over 1000 °C [5]. Moreover, many solid materials are involved in high temperature chemical processes, allowing Thermochemical Energy Storage (TCES). This consists in exploiting concentrated solar energy to drive an endothermic reaction, producing valuable energy carriers. As a matter of fact, the chemical products have a higher enthalpy than the reactants and can release it through an exothermic reaction. These energy carriers do not need to be kept at high temperature and so they can be stored for an unlimited time. More in general solar-driven endothermic reactions can be performed to produce sustainable fuels, chemicals, and materials, opening new scenarios for CST technologies.

1.1. *Solar-driven thermochemical processes*

Solar energy can be exploited for the production of energy carriers and materials through innovative and traditional processes [6]. Many TCES processes involve cycles of two or more reactions, by which a reactant is regenerated and recycled to the initial step [7]. A category is represented by sorption cycles, by which concentrated solar energy sustains the desorption of a gaseous compound from a solid sorbent, through an endothermic chemical reaction. Then, stored energy can be released on demand through the reverse adsorption reaction, fixing again the gaseous compound on the sorbent. This is the case of the Calcium Looping process, which is also of interest for Carbon Capture [8]. Calcium oxide (CaO) is used as chemical sorbent to remove carbon dioxide (CO_2) from flue gas streams producing calcium carbonate ($CaCO_3$) at 650–750 °C. CaO is regenerated separately by the reverse reaction above 900 °C, producing a pure CO_2 stream. This process is an ideal candidate for TCES, due to the large enthalpy change of the reaction ($\Delta H_{298} = 178$ kJ/mol) and the availability of limestone as a cheap natural source [9]. Different materials, including synthetic sorbents, have been studied to achieve high storage densities [10,11]. Redox cycles can be implemented to produce synthesis gas, namely hydrogen (H_2) and carbon monoxide (CO), that can be used as fuels [12]. These processes involve two heterogeneous reaction steps, in which an oxygen carrier (generally a metal oxide) is cyclically reduced and oxidized. Thermochemical splitting of water (H_2O) or CO_2 can be performed in this way. Solar energy can sustain the reduction of the oxygen carrier, releasing oxygen (O_2). Then, the reduced oxide reacts with H_2O or CO_2, producing H_2 or CO and regenerating the oxygen carrier. The thermal reduction typically requires temperatures of 1000–1500 °C and extremely low O_2 partial pressures. Methane (CH_4) can be used as reducing agent to lower the reduction temperature at 900 °C and to enhance the production of syngas (Chemical Looping Reforming) [13]. The selection of oxygen carriers is a challenging research field [14,15]. Volatile oxides release metal vapours, when reduced. The separation of the metal from the exit gas stream is a critical step, to avoid the recombination with O_2 [16]. On the other hand, non-volatile oxides do not release gaseous species, when reduced. This is the case of magnetite (Fe_3O_4), the first oxide proposed for solar-driven thermochemical splitting [17]. Mixed oxides have also been investigated like ferrites [18], aluminates [19] and perovskites [20]. Non-stoichiometric oxides offer several advantages: moderate temperatures of reduction, fast kinetics of re-oxidation and good stability over cycles. Ceria (CeO_2) is a reference material of this kind [21]. Perovskites also belong to this category [22,23]. Solar fuels can be also produced through the thermochemical conversion of carbonaceous feedstocks (either fossil or bio-based). Solar gasification is a long studied process, involving the endothermic reaction of the feedstock with H_2O (or CO_2) at very high temperatures 900–1400 °C [24]. The use of solar energy brings several advantages compared to the traditional autothermal process, in which a considerable part of the feedstock is burnt to supply the reaction heat. However, for all the mentioned thermochemical processes, there is a need to increase the solar-to-fuel efficiency and thus the process overall efficiency. In this scenario, the solar reactor design and heat recovery operation are key factors to improve the efficiency [25,26].

1.2. *Solar reactors*

The promising outlook for the application of CST technologies to chemical processes has prompted researchers to devise new reactor concepts, combining the principles of chemical and solar engineering [27]. The task of heating a solid with a concentrated solar flux can be fulfilled with various technical solutions common to particle receivers [28]. In indirectly irradiated systems an intermediate element absorbs solar radiation and heats the particles by conduction or re-emission. In directly irradiated systems, the particles are exposed to the concentrated sunlight, passing through an optical aperture. The aperture is usually closed by a transparent window, to collect the outlet gas and to minimize convective losses. According to the multiphase flow regime, solar reactors and particle receivers are divided into stacked, entrained, and fluidized beds. Fixed bed reactors benefit from low costs and easy operability. A relevant example is the indirectly irradiated packed bed reactor, developed at the Paul Scherrer Institute (PSI) [29,30] and tested at the 300 kW solar furnace of the Weizmann Institute of Science (WIS) [31]. Rotary kilns are praised for good solid mixing, flexibility and simple control and were proposed to be coupled with CST technology for the first time in 1980 [32]. They can process solids within a wide range of particle sizes in continuous modality. A directly irradiated rotary kiln has been developed at the German Aerospace Center (DLR) with a throughput of 10 kg/h [33]. A directly irradiated rotating cavity reactor has also been developed at the PSI [34,35] and tested at the solar furnace of the French National Centre for Scientific Research (CNRS) in Odeillo with a power input of 100 kW [36]. Directly irradiated free-falling particle receivers have been studied for forty years at the Sandia National Laboratories (SNL) [37]. They can heat large amounts of solids with short exposure times [38] but have not been so far employed as solar reactors. The lack of a window closing the aperture is the main technical issue, causing large energy losses and wind disturb [39]. The solar vortex flow reactor developed at the PSI must be mentioned among entrained beds [40]. A continuous stream of fine solid particles is entrained in a cylindrical cavity by a gas vortex flow. A modified design has been proposed by the University of Adelaide, featuring a conical inlet located at the opposite side of the aperture of the cavity [41]. This configuration generates an expanding vortex flow, that mitigates particle deposition on the window and causes the recirculation of larger particles, increasing their residence time and conversion degree [42].

Thanks to their excellent heat transfer properties, fluidized beds have also been recognized as a suitable solution for the absorption of concentrated solar energy very early in the 1980s [43], and in the last ten years the development of fluidized bed solar receivers and reactors has seen an acceleration thanks to innovative designs [44,45]. Good thermal diffusivities allow to spread the heat from the irradiated spot to the entire volume of the reactor [46]. Uneven fluidization can enhance thermal diffusion and reduce convective energy losses [46–48]. This principle underlies the design of the internally circulating fluidized bed investigated at the University of Niigata [49,50], and of the spouted bed tested at the CNRS [51]. The internally circulating fluidized bed reactor has been scaled-up and has started to be tested at the 100 kW beam-down solar furnace of the University of Miyazaki. The idea of uneven fluidized beds has been explored and pushed further by the University of Naples Federico II and the Italian National Research Council (CNR) with the compartmented fluidized bed receiver, designed to perform the different tasks of CST energy collection, storage and supply in a single unit [48,52]. This concept has been demonstrated in two commercial pilot plants [53], built and successfully operated by the Italian company Magaldi, one rated at 100 kW, the other at 2 MW peak radiative power.

Indirect heating configurations have also been proposed, exploiting the large bed-to-wall heat transfer coefficients of dense suspensions. A pair of twin indirectly irradiated fluidized bed reactors has been tested at the 10 kW solar furnace of the National Renewable Energy Laboratory (NREL) [54]. Dense circulating systems have been developed, both with up- [55] and downflowing bubbling fluidized bed receivers [56], to have a continuous throughput of heated particles. The upflowing bubbling fluidized bed concept is being now tested at the 4 MW Themis solar furnace [57]. Finally, in order to improve the control of the residence time of the solid, a cross-flow fluidized bed composed of multiple horizontal stages has been proposed [58] and a 50 kW prototype has been tested at the CNRS [59].

1.3. *The directly irradiated fluidized bed autothermal reactor*

Heat recovery has been pointed out as a key strategy to increase the efficiency of thermochemical cycles for hydrogen production through analytical models [25,60]. Falter and Pitz–Paal modeled a heat exchanger operated in the countercurrent mode with CeO_2 particles [61]. Such examples show how the recovery of the sensible heat of the products, according to the principle of an autothermal reactor, can improve the efficiency of solar-driven chemical processes and set a technological advance in this field. However, no attempt has yet been made in the development of a solar autothermal reactor. For this reason, the Authors have proposed a new type of solar reactor, named Directly Irradiated Fluidized Bed Autothermal Reactor (DIFBAR) [62].

The DIFBAR is composed of a conical cavity receiver connected at the bottom to two vertical coaxial tubes (Fig. 1). The bed material is fed to the receiver through the inner tube (the riser), that is operated as a fluidized bed riser. There, the particles are exposed to a high flux of solar radiation and undergo a chemical reaction at high temperature. Then, they separate from the gas stream and fall into the outer tube (the annulus), that is operated as an overflow standpipe. The material descends through the annulus as a moving bed and transfers its sensible heat to the granular suspension flowing up through the riser. In this way a thermochemical process can be carried out continuously and the sensible heat of the solid products is recovered to preheat the feed. Two alternative plant schemes are considered. In the “Dual Tank” scheme the stream of processed solid is collected in separate tanks (Fig. 1, left). The reacted material can be sent to a reactor for the exothermic reaction of material regeneration and then returned to the feed tank. In the “Single Tank” scheme (Fig. 1, right), the solid material is continuously recirculated between the receiver and a single reservoir, that can eventually be operated to perform the exothermic reaction. When the reservoir is operated as a storage tank, the mixing of the product and the reactant solids should be avoided, to prevent the reacted solid to be sent back to the receiver. Segregation of reacted and unreacted particles is possible when the reservoir is operated as a moving bed: the reacted particles descending from the annulus are collected on the top of the reservoir, while feeding of unreacted particles to the riser occurs from the bottom of the reservoir (Fig. 1-right). Differently, if the reservoir is employed as a reactor, fluidized bed conditions might be preferable. In any case this design has the advantage of reducing the plant volumes. Gas by-passing from the reservoir to the receiver or vice versa is undesired and must be avoided by a proper design and control.

A Single Tank prototype was tested with a high-flux solar simulator, to investigate the performance of the heat exchanger. Very favorable overall heat transfer coefficients were found, ranging between 400 and 700 $W\ m^{-2}\ K^{-1}$ though the experiments were performed at relatively low temperatures [62]. A smaller experimental test rig, then, was tested at higher temperatures, relevant to TCES applications [63]. However, the design of this reactor prevented the full demonstration of the heat exchange section. With the data obtained from these experiences, theoretical calculations based on thermodynamic equilibrium were performed to find the optimal length of the heat exchanger in TCES conditions [64]. Calcium Looping was taken as case-study, though the DIFBAR can be potentially employed for any thermochemical process. The thermal efficiency of the reactor was evaluated as the ratio between the energy stored through the reaction and the net energy absorbed by the particles. Calculations show that a maximum efficiency close to 90% could be attained operating the receiver with a temperature of about 900 °C. The optimal length of the heat exchanger depends on the circulation rate of the solid. For a chosen length of 1 m, the reactor should be operated with a circulation flowrate of 1.4 g/s. Based on these results, a new prototype was built to fully demonstrate the autothermal principle. This paper reports the first experimental results. The hydrodynamics of the system is studied at ambient temperature with inert sand as a preliminary step. Solids and gas by-passing flowrates are assessed to

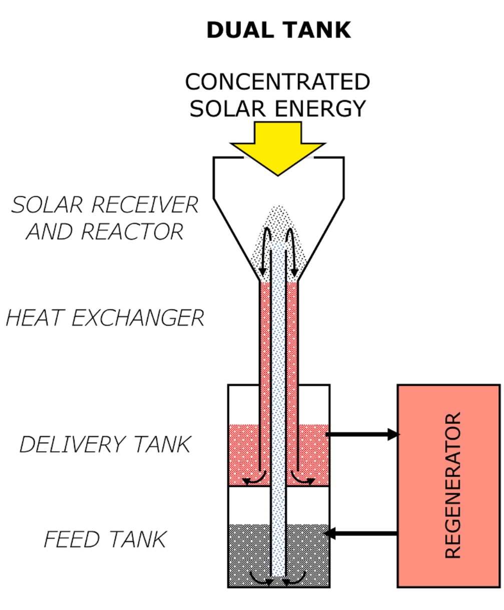

Fig. 1. Outline of the DIFBAR. Alternative schemes: dual tank (left) and single tank (right).

verify the achievement of design objectives and the effects of control variables are studied through the analysis of the pressure loop. Operative temperatures are assessed with the same inert sand, heating the reactor with a high-flux solar simulator. Steady state temperature profiles have been analyzed to assess the performance of the heat exchanger. The operability of a solar-driven chemical process has been proved by calcining a batch of magnesium carbonate ($MgCO_3$) particles, added to the inventory.

2. Methods

2.1. Experimental set-up

2.1.1. The DIFBAR

Fig. 2 shows a schematic of the experimental apparatus. The prototype is mainly composed of five parts aligned along a same vertical axis: i) the riser tube, internal diameter (ID) 10 mm, length 1490 mm; ii) the annulus tube, ID 20.9 mm, length 1000 mm; iii) the receiver, upper ID 102.3 mm, length 135 mm, lower internal cone angle 30°; iv) the reservoir, ID 77.9 mm, length 225 mm; v) the standpipe, ID 20.9 mm, length 100 mm. All the parts are made of stainless steel (AISI 310 and AISI 316). The annulus ends are welded directly at the conical bottom of the receiver and at the top flange of the reservoir. The annulus tube is interrupted by four flanged connections, so that three segments can be removed and replaced: a 225 mm segment can be removed to insert a second reservoir for the “Dual Tank” configuration; a 120 mm segment can be replaced with an identical piece made of Plexiglas, to observe the flow through the annulus in cold flow experiments. The receiver is sealed at the top by a circular window, 140 mm diameter, 4 mm thick. The standpipe is welded at the bottom flange of the reservoir and connected to the riser by a reducer fitting. The riser protrudes inside the receiver for 35 mm. The solid returns to the riser through four symmetrical orifices (6 mm) at a height corresponding to the bottom of the standpipe.

A fluidizing gas stream (Q_1) is fed to the riser, through a nozzle (ID 4 mm). A secondary gas stream (Q_2) can be fed to the reservoir, through a single-ring sparger with seven holes (1 mm), made of a copper bent tube (ID 8 mm). Two additional gas streams can be fed to the lower segment of the annulus (Q_3) and to the standpipe (Q_4) right below the reservoir from two symmetrical tubes (ID 4 mm), to provide a gas-sealing for the reservoir and the receiver. The Q_3 stream also allows an independent control of the solid discharge from the annulus into the reservoir, thanks to a disk of 50 mm, fixed on the riser 4 mm below the annulus: when the Q_3 stream is off, the granular solid inside the annulus lays as a fixed bed, sustained by the disk; when the Q_3 stream exceeds a minimum flowrate, the particles are dragged by the gas and fall into the reservoir. This behavior closely resembles the operation principle of an L-valve.

The reactor has been thermally insulated with multiple layers of rock wool blanket and ceramic fiber half-shells for the high temperature experiments. The solar simulator consists of a short-arc Xe lamp coupled with an elliptical reflector. Lamp input power can be tuned from 2 to 9 kW_e, with 1 kW_e increments. Two semi-cylindrical ceramic fiber heaters (Watlow), placed around the reservoir and connected in series, are used to speed up the heating phase. The power of the heaters is controlled between 0 and 1.5 kW with a TRIAC (Sylvania), manually regulated by a potentiometer.

2.1.2. Materials

The bed inventory consists of 1.2 kg of quartz sand. The mean Sauter diameter of the particles is 150 μm (size range: 80–300 μm) and the density is 2600 kg/m^3 (Geldart class B). The minimum fluidization velocity has been assessed experimentally in a Plexiglas column (ID 40 mm) using air as fluidizing gas and is about 1.9 cm/s. A magnesium carbonate ($MgCO_3$) powder (96.6% $MgCO_3$ content in the raw sample, size range: 300–400 μm) was added to the sand inventory for calcination experiments.

Air was used for the operative gas streams, supplied by an outdoor gas compressor. CO_2 from a technical cylinder (99.9% purity) was used for gas tracing experiments.

2.1.3. Measurement and control instrumentation

The gas was fed with mass flow controllers from Bronkhorst (El-Flow® Select series). Eight pressure transducers from Keller-Druck (full scale of 100, 200 and 500 mbar) and sixteen K-type thermocouples are

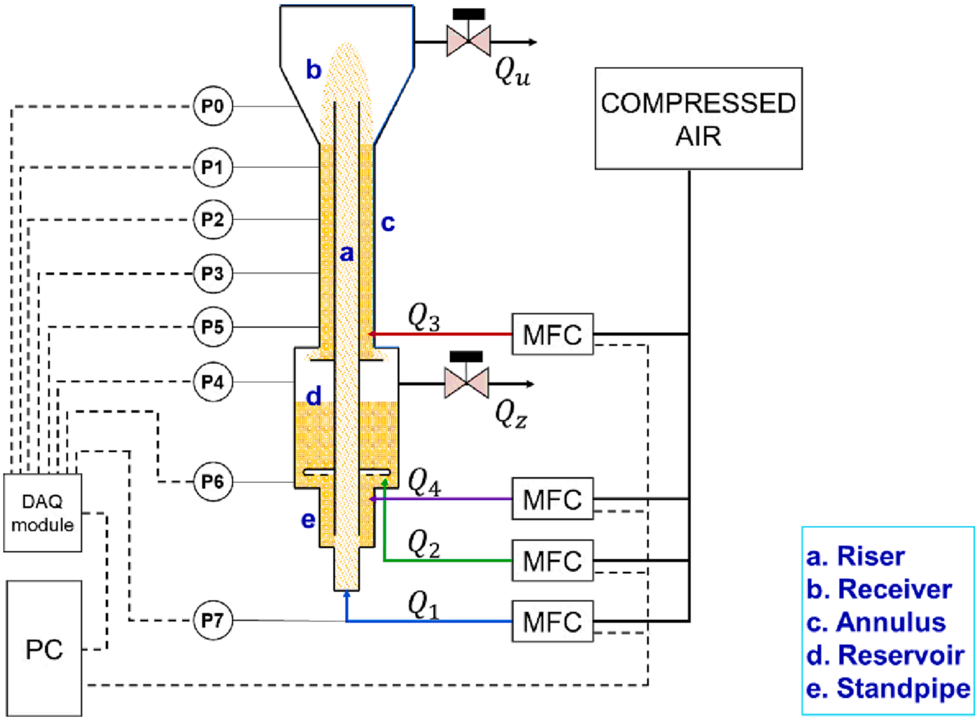

Fig. 2. Schematic of the experimental apparatus.

installed at various heights through lateral ports. The exact positions of the pressure transducers and the thermocouples are reported in Table 1, where the bottom of the receiver is taken as reference for the vertical coordinate. The position of the instrument is also depicted in Figs. 2 and 3. In order to measure riser temperatures, some thermocouples (T1, T6, T8, T9, T13 and T14) touch the outer wall of the riser tube. The small thickness (1 mm) and the high thermal conductivity of the stainless-steel tube ensure a negligible temperature difference across the wall, allowing a reliable measurement of the internal riser temperature through its outside wall temperature.

The voltage signals from transducers and thermocouples were acquired with the NI 9201 and 9213 acquisition modules, respectively, connected to a desktop PC with a NI cDAQ 9174 chassis. A LabView application was used both to record the pressure measurements and to manage the set points of the mass flow controllers. A digital feedback control algorithm was implemented through the application to keep the bed level in the annulus at the maximum height, by automatically adjusting the set point of Q_3. The bed level is assessed as the intercept of the pressure profile along the annulus. Two needle valves from DK-LOK (orifice 9.5 mm) on the outlet tubes (ID 10 mm) regulate the exit pressure drops. A piston check valve from VYC Industrial was installed on a lateral tube of the receiver, with an opening pressure of 80 mbar, to protect the window from breakage by overpressure.

2.2. Experimental procedure

2.2.1. Solid circulation rate

The solid circulation rate (W) was determined at ambient temperature by two methods. In a first set of experiments, Q_3 was set off, so the annulus bed could not be discharged into the reservoir, and the bed level in the annulus increased. The mass flowrate of the solid flowing through the riser and settling in the annulus could then be calculated, by measuring with a stopwatch the time required to fill the Plexiglas segment between −165 and −75 mm (reference origin at receiver/annulus connection). The bed mass contained in the Plexiglas segment was independently measured by filling it with the bed material. At least five independent tests were run for each condition. By these experiments W was obtained for both the conditions of open receiver and receiver closed by the window.

A second set of experiments was performed under stable and steady circulation conditions, obtained when the solid mass flowrate in the riser is equal to that discharged from the annulus section. The first one is mainly regulated by the gas flowrate in the riser, Q_1, whereas the Q_3 gas flowrate controls the discharge flowrate of the moving bed in the annulus. A constant level of the bed in the annulus is reached at steady state conditions and, for the optimal autothermal operation, it should be kept at the maximum height. For any circulation condition, a small paper basket with a funnel shape was lowered at the bottom of the receiver to collect the particles flowing out of the riser for a pre-set time interval. Then, by weighing the sample, the mass flowrate could be calculated. At least five independent tests were run for each condition. For these measurements, the receiver had to be open. The results of the two methods match very well, so the first method was assumed to be reliable.

Table 1
Position of measuring instruments.

z [mm]	Pressure transducers	Thermocouples			
44	P0	Receiver	T10	Riser	T11
−20	–	Annulus	T12		T9
−260	P1		–		T8
−510	P2		T7		T13
−760	P3		–		T6
−980	P5		T5		T14
−1091	P4	Reservoir	–		T15
−1159	–		T4		
−1231	P6		T3		T0
−1266	–	Standpipe	T2		T1
	P7	Inlet nozzle			

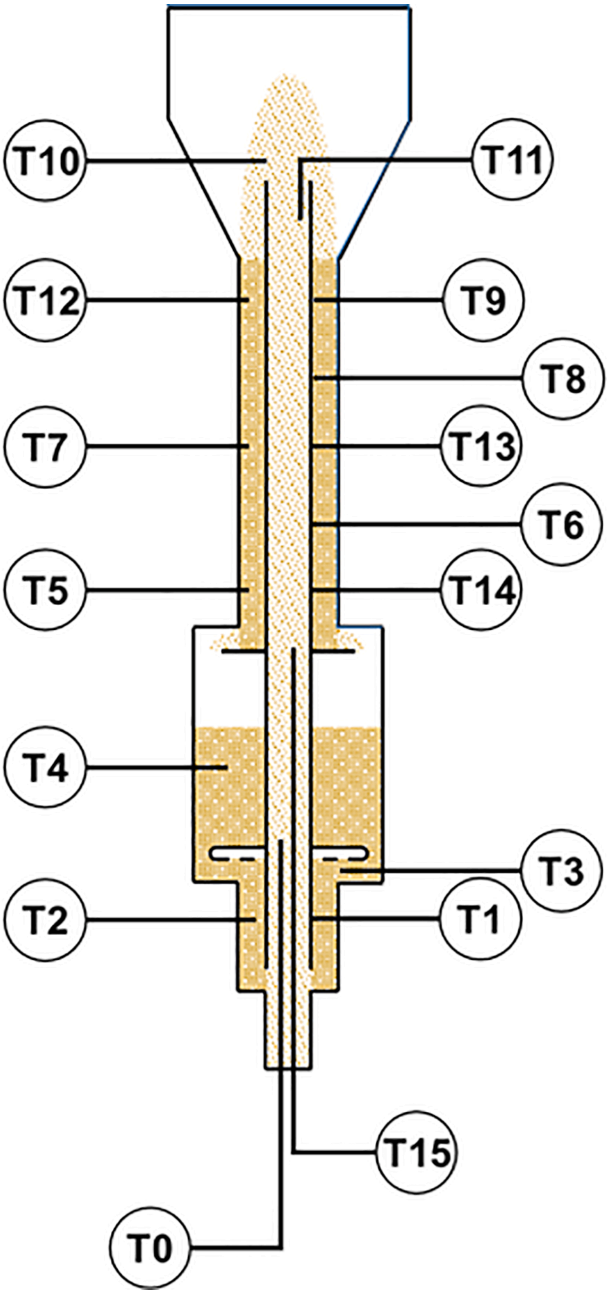

Fig. 3. Schematic of thermocouples arrangement.

2.2.2. Pressure loop

The pressure loop data were recorded during the gas tracing tests. Transducers were carefully calibrated with an external pressure regulator before each test. The pressure at the bottom of the riser could not be measured and was estimated as following: the pressure drop across the nozzle was measured in absence of the bed material at different flowrates of Q_1. The obtained values were subtracted from the corresponding measurements during the circulation experiments.

2.2.3. Gas by-passing

Gas streams can flow through the annulus (Q_a) and the standpipe connections (Q_c), as shown in Fig. 4. These streams can either flow

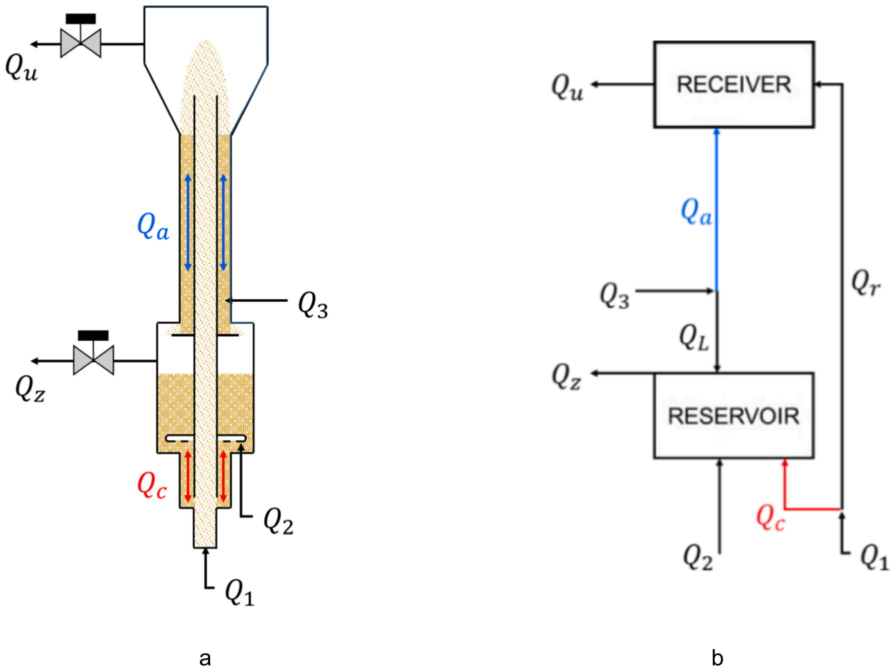

Fig. 4. Gas by-passing streams depicted in the reactor sketch (left) and block diagram (right).

upward or downward. Depending on its direction the Q_a stream can cause a dilution or a loss of the gaseous products from the receiver. The Q_c stream, instead, can cause a dilution or a loss of the gaseous reactants fed to the riser. The two connections were carefully designed to minimize the two by-pass flows.

A series of experimental tests were carried out to understand the direction and intensity of these two streams. In these experiments CO_2 was used as a gas tracer, continuously mixed with one of the three inlet streams (Q_1, Q_2 and Q_3). Q_4 was always off in these experiments. An ABB AO2020 Uras 26 gas analyzer (CO_2: 0–20%) measured the concentrations of the tracer alternatively from the receiver and the reservoir outlets (y_u and y_z, respectively). A pump (KNF N814KTE) sucked a fixed gas flowrate (45 L/h) for the analyzer from one of the two outlets through a tee connection.

Since Q_a and Q_c may have a different direction according to the operating conditions, they are referred to as quantities with a sign. As convention, they will be considered positive if directed upward (Fig. 4b) and negative if directed downward. In this sense, an increase of these quantities must not be understood necessarily as an increase in absolute value.

2.2.4. *High temperature experiments under inert conditions*

Heating experiments under inert conditions were performed to assess the performance of the heat exchanger. The first heating test was conducted without the assistance of the reservoir heaters, to observe the time evolution of the temperatures obtained by pure irradiation with the lamp power fixed at minimum value (2 kW_e). The temperature profile of the heat exchanger was obtained by measuring the temperatures of the sand in the annulus and the riser wall temperatures. Then, successive tests were conducted to assess the reactor temperatures for higher irradiation powers. The reservoir heaters were used to speed up the heating phase and then switched off, to obtain steady state temperature profiles by pure irradiation.

For each experimental test at specific input power, the power transferred in the heat exchanger (P_{ex}) and the power absorbed in the receiver (P_{rec}) were evaluated on the basis of the measured temperature loop profile. In particular, assuming the system adiabatic, P_{ex} was estimated considering the temperature decrease in the annulus from T_{12} to T_5:

$$P_{ex} = Wc_{p|[T5;T12]}\Delta T_a \tag{1}$$

$$\Delta T_a = T_{12} - T_5 \tag{2}$$

Instead, P_{rec} was calculated by:

$$P_{rec} = Wc_{p|[T9;T12]}\Delta T_{rec} \tag{3}$$

$$\Delta T_{rec} = \Delta T_{ex} \tag{4}$$

where the temperature variation of solid particles from the inlet and the outlet of the receiver was estimated considering the mean value of the temperature differences between the riser and the annulus (ΔT_{ex}) at different heights. ΔT_{ex} was evaluated by:

$$\Delta T_{ex} = [(T_{12} - T_9) + (T*_8 - T_8) + (T_7 - T_{13}) + (T_5 - T_{14})]/4 \tag{5}$$

where $T*_8$ is the arithmetic mean temperature between T_{12} and T_7.

Finally, the overall heat transfer coefficient can be calculated by:

$$U = P_{ex}/(A\,\Delta T_{ex}) \tag{6}$$

It is noteworthy that since the solid streams rising in the riser and descending in the annulus have the same mass flowrate and heat capacity, the temperature difference along the heat exchanger should be constant [62]. Therefore, the use of a mean value of temperature difference, rather than a logarithmic mean, is permitted in Eq. (6). The formulas for the evaluation of specific heats and enthalpies have been taken from [65].

On the basis of the previous calculations, a heat recovery factor (*R*) can be evaluated as:

$$R = P_{ex}/(P_{ex} + P_{rec}) \tag{7}$$

2.2.5. *High temperature experiments under reactive conditions*

Two calcination experiments were conducted to test the operability of the DIFBAR prototype as a solar reactor. A batch of $MgCO_3$ particles was loaded in the reactor and mixed with the sand inventory for a mass fraction of 8.0%. The reactor was then heated with the lamp power set at maximum power (9 kW_e). The reservoir heaters were used only during the initial transient heating, to speed up the achievement of steady state conditions. An ABB AO2020 Uras 14 gas analyzer (CO_2: 0–100%) measured the concentration at the outlet of the receiver and data points are acquired with a sampling rate of 1 Hz.

The calcination rate ($\dot{n}$) is calculated from the CO_2 concentration in the receiver outlet gas (y_u) as:

$$\dot{n}(t) = (Q_1/V_N)\ y_u(t)/[1 - y_u(t)] \tag{8}$$

where V_N is the normal molar volume of an ideal gas.

Then, the global conversion degree (X_g) can be obtained by the integral:

$$X_g(t) = \int_0^t \dot{n}(t')\ M_{MgCO3}\ dt'/(m\ \alpha_0) \tag{9}$$

where M_{MgCO3} is the molar mass of $MgCO_3$, m is the total inventory mass and α_0 is the initial mass fraction of the solid reactant. As the receiver is operated as a continuous reactor, it also possible to assess the time-resolved conversion degree (X_f) in the receiver as:

$$X_f(t) = \dot{n}(t) M_{MgCO3}/[W\ \alpha(t)] \tag{10}$$

where α(t) is the instantaneous mass fraction of the solid reactant at the inlet of the receiver and must be updated with time. As a rough estimate, α(t) can be calculated as the mean mass fraction, assuming perfect mixing conditions for the solid phase in the whole system:

$$\alpha(t) = \alpha_0 [1 - X_g(t)] \tag{11}$$

At last, the heat recovery factor under reactive conditions can be reformulated as:

$$R = P_{ex}/[P_{ex} + P_{rec} + \dot{n}(t)\Delta H^\circ] \tag{12}$$

where ΔH° is the standard molar enthalpy change of the reaction at 600°C: 109 kJ/mol.

3. Results

3.1. Solid circulation rate

Fig. 5 reports the mass flowrate of the circulating solid particles (W), and the corresponding mass flux with respect to the riser section (G_r), as a function of the superficial velocity u_1 of the gas fed to the riser at ambient temperature. When u_1 is increased, the solid circulation rate generally increases with a linear trend. A maximum value close to 2 g/s is asymptotically approached above 1.5 m/s, when the reservoir is not aerated. This limit disappears when the reservoir is aerated, and the pressure is increased either by increasing the flowrate or by increasing the outlet pressure drop of the reservoir.

A minimum feed velocity in the riser of about 1.1 m s^{-1} is needed to have the solid circulation. The height reached by the particles ejected inside the receiver increases with u_1, but the operative velocity range is limited to prevent the particles to impact the window. By increasing u_1, the transition from the slugging to the fast-fluidization regime is visually observed, as at low velocities the particles are ejected into the receiver with intermittent slugs, whereas at higher velocities a fountain-like jet becomes stable, as already observed in previous studies [63].

3.2. Pressure loop

Fig. 6 shows the time-averaged pressure profiles along the vertical axis of the DIFBAR obtained during the experiments for fixed values of u_2, while varying the riser velocity u_1 between 1.3 and 1.5 m/s. By

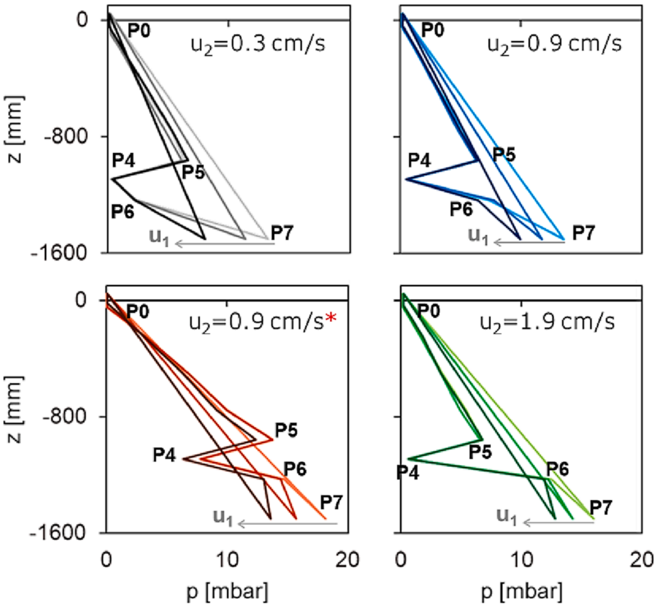

Fig. 6. Pressure profiles along the vertical axis of the DIFBAR for fixed values of u_2 while varying u_1. The condition labelled with the asterisk (*) was obtained by partially closing the reservoir outlet valve.

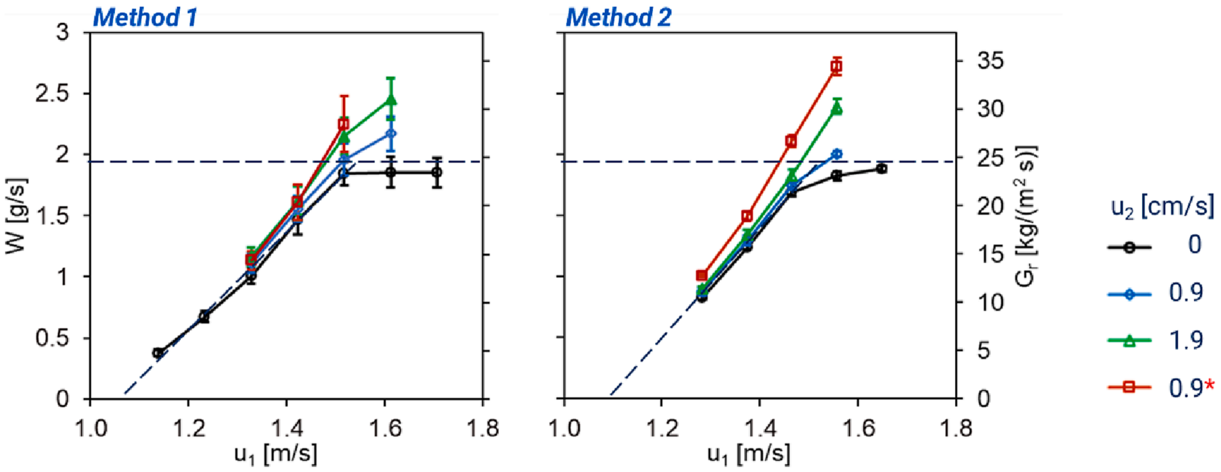

Fig. 5. Mass flowrate W of the circulating solid particles as a function of the riser feed velocity (u_1) at ambient temperature for different values of the reservoir gas velocity (u_2) with the two methods: annulus level rise timing (left) and riser outlet sampling (right). The condition labelled with the asterisk (*) was obtained by partially closing the reservoir outlet valve.

increasing u_1, the bottom pressure of the riser P7 decreases, suggesting that the solid hold-up of the riser is reduced. Consequently, the pressure drop between the riser and the reservoir ($\Delta p_c = P7 - P6$) decreases, indicating a decrease of Q_c. By increasing u_2, the bottom pressure of the reservoir P6 increases. Also in this case, Δp_c is reduced. Then Q_c can be largely decreased in this way. The same reduction of Δp_c can be obtained by partially closing the outlet valve of the reservoir, thus increasing both P4 and P6, but in this way it is possible to keep the reservoir in non-fluidized conditions. P5 also increases because the pressure drop through the L-valve ($\Delta p_L = P5 - P4$) remains almost constant. Consequently, the pressure drop in the annulus ($\Delta p_a = P5 - P0$) increases, indicating an increase of Q_a.

3.3. Gas by-passing

The pressure loops give a qualitative understanding of the effect of feed flowrates on the gas-bypassing streams Q_a and Q_c. However, no indication about their sign and intensity can be directly obtained. The gas tracing experiments were aimed at investigating these aspects (see Fig. 4).

In a first set of experiments, the tracer was introduced in the Q_3 stream with a fixed flowrate of 10 NL/h (for an inlet concentration y_3 of about 50%) and the receiver outlet concentration y_u was measured. For each condition, except when the outlet valve is partially closed, the concentration was equal to that measured in air ($y_{air} = 0.04\%$), as shown in Fig. 7-left, indicating that Q_a is always negative: it flows from the receiver downward along the annulus, dragged by the moving bed, and joins the Q_3 stream.

Then, the tracer was introduced in the Q_2 stream with a concentration of about 20%. Fig. 7-right shows the y_u concentration for each condition. As it can be seen, in almost every case y_u is equal to y_{air}, indicating that Q_c is positive: it flows from the riser up to reservoir through the standpipe. Differently, when the reservoir is fluidized ($u_2 \geq 1.9$ cm/s) or the outlet valve is partially closed, the direction of Q_c is reversed by the increase of u_1, since the tracer reaches the receiver ($y_u > 0.04\%$). This is coherent with the results of the pressure loops, indicating the decrease of Q_c. This is also a very useful result, indicating the possibility of zeroing the Q_c by-passing stream by regulating the pressure of the reservoir.

At last, the tracer was introduced in the Q_1 stream and both outlet concentrations (y_u and y_z) were measured. Knowing both the outlet concentrations, the outlet flowrates from the receiver (Q_u) and the reservoir (Q_z) can be calculated from the global balances:

$$\sum_{i=1:3} Q_i = Q_u + Q_z \tag{13}$$

$$\sum_{i=1:3} Q_i y_i = Q_u y_u + Q_z y_z \tag{14}$$

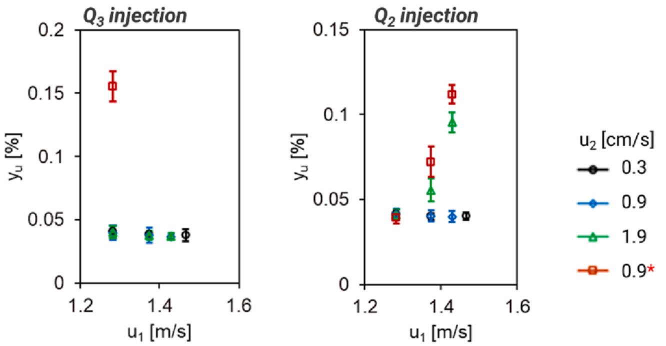

Fig. 7. Receiver outlet concentration y_u for experiments with injection of the tracer in the Q_3 (left) and Q_2 (right) streams. The condition labelled with the asterisk (*) was obtained by partially closing the reservoir outlet valve.

Ideally, if no by-passing occurred across the two standpipes, $Q_u = Q_1$ and $Q_z = Q_2 + Q_3$. The outlet flowrates are reported in Fig. 8 in the form of dimensionless ratios, by dividing them with their ideal value. As it appears, the deviations from the ideal ratio of 1 are small, suggesting that the by-passing flowrates are small, though not proving it.

Unfortunately, gas tracing measurements do not provide further information to solve the internal mass balances. However, the by-passing flowrates Q_a and Q_c can be assessed by the following procedure. The relative gas–solid velocities are calculated from the pressure gradient along the two standpipes according to the law of Ergun:

$$\Delta p \big/ L = 150\left[(1-\varepsilon)/\varepsilon\right]^2 \mu\, u_i \big/ d_p^2 + 1.75\left[(1-\varepsilon)/\varepsilon\right] \rho\, u_i^2 \big/ d_p \tag{15}$$

where ρ is the gas density, μ is the gas viscosity, d_p is the particle diameter, ε is the voidage and u_i is the interstitial relative gas–solid velocity. Then, the absolute superficial gas velocity u_g is obtained by the definition of the relative velocity:

$$u_i = u_g/\varepsilon - G_s\big/\left[\rho_s(1-\varepsilon)\right] \tag{16}$$

where G_s is the solid mass flux and ρ_s is the particle density. Both u_g and G_s must be taken as quantities with a sign and the same convention is applied: upward flows are positive.

Fig. 9 shows the results of the calculations in terms of gas by-passing flowrates Q_a and Q_c through the annulus (left) and the standpipe (right) as a function of the riser velocity, for fixed values of u_2.

The pressure gradient through the annulus does not sensibly change with gas velocities u_1 and u_2 but is considerably affected by the reservoir outlet pressure P4 (Fig. 5). As a result, the trends of Q_a mainly depend on the solid mass flux: as the circulation rate W increases, the by-passing rate Q_a is predicted to decrease (Fig. 9-left). All calculated values agree with the evidence of a negative Q_a, except when the outlet valve is partially closed. The decreasing trends of Q_c (Fig. 9-right), instead, are as expected from the pressure loops and the signs agree with the tracing experiments.

3.4. High temperature experiments

3.4.1. Operation under inert conditions

When performing the high temperature experiments, the hydrodynamics of the reactor slightly changes. The major effect is that the riser gas velocity increases along the axial coordinate because of thermal expansion. As a consequence, the riser exit velocity is higher than the

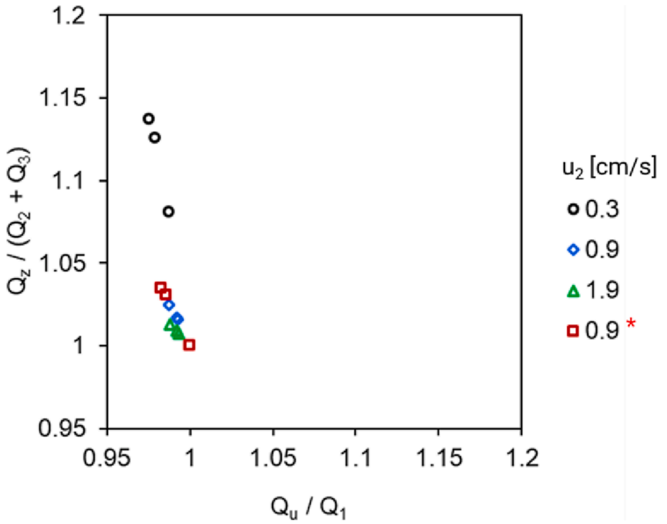

Fig. 8. Normalized outlet flowrates as calculated from global balances. The condition labelled with the asterisk (*) was obtained by partially closing the reservoir outlet valve.

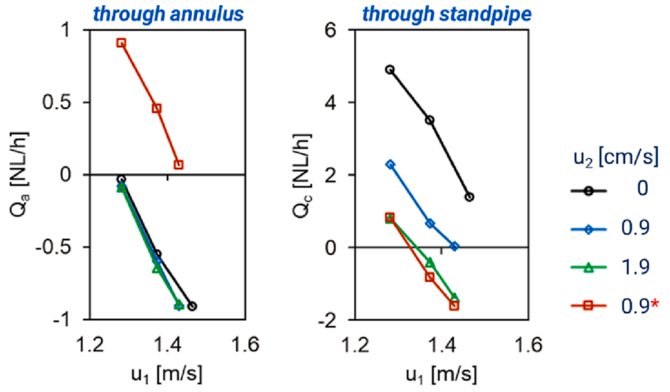

Fig. 9. Calculated gas by-passing flowrates as a function of the riser velocity for fixed values of u_2: left) Q_a; right) Q_c. The condition labelled with the asterisk (*) was obtained by partially closing the reservoir outlet valve.

inlet one. According to the ideal gas equation of state, the gas velocity linearly increases with the temperature and the ratio between the exit (u_{rf}) and inlet (u_{r0}) velocity is given by:

$$u_{rf}/u_{r0} = T_{rf}/T_{r0} \tag{17}$$

where T_{rf} is the temperature at the exit of the riser and T_{r0} that at the entrance. The first visible consequence is the increase of the height of the particles jet inside the receiver for a fixed inlet velocity. Therefore, the inlet operating velocity must be limited to prevent impacts with the window. On the other hand, the inlet velocity cannot be lower than the minimum circulation velocity (u_{min}). As a result, the operative range becomes narrower. When the bottom temperature (T_{r0}) is close to ambient temperature (about 300 K), an increase of 300 K along the heat exchanger determines an increase in the riser velocity by a factor $u_{rf}/u_{r0} = 2$. For this reason, it was preferable during the first test to work close to the minimum circulation velocity and with the minimum lamp power: in particular, the inlet riser velocity was $u_{r0} = 1.2$ m/s and the lamp power was 2 kW_e. The time evolution of reactor temperatures for the first test is shown in Fig. 10.

The solar simulator is powered on at time zero. Temperature profiles have been smoothed with a three-minutes moving average. The thermocouples in the receiver evidence a very rapid heating (over 100 °C/min), but their measurement is probably affected by the absorption of the concentrated radiative flux. Initial heating rates become smaller, by moving down along the annulus. At the bottom of the heat exchanger, the temperature increase appears delayed by 15 min. Over time, heating rates increase at the bottom of the heat exchanger and decrease at the top. As a consequence, the shape of the temperature profile changes with time (Fig. 11). It takes between 1 and 2 h to achieve a uniform heating rate along the heat exchanger. Correspondingly, the temperature profile assumes the classical parallelogram shape, which proves the correct design and operation of the heat exchanger.

The mean temperature difference between the riser and the annulus is $\Delta T_{ex} = 18.5$ K, the temperature increase along the heat exchanger is $\Delta T_a = 169$ K, and a heat recovery factor (*R*) of 90% was calculated. This means that 90% of the heat duty to heat the solid at the temperature of the receiver is recovered by the heat exchanger. The solid circulation rate required to calculate P_{ex} and U (Eqs. (1) and (6)) was determined by cold flow data (Fig. 5), taking as reference the velocity at the riser mid-height ($u_1 = 1.4$ m/s, W = 1.2 g/s). The heat transfer coefficient results

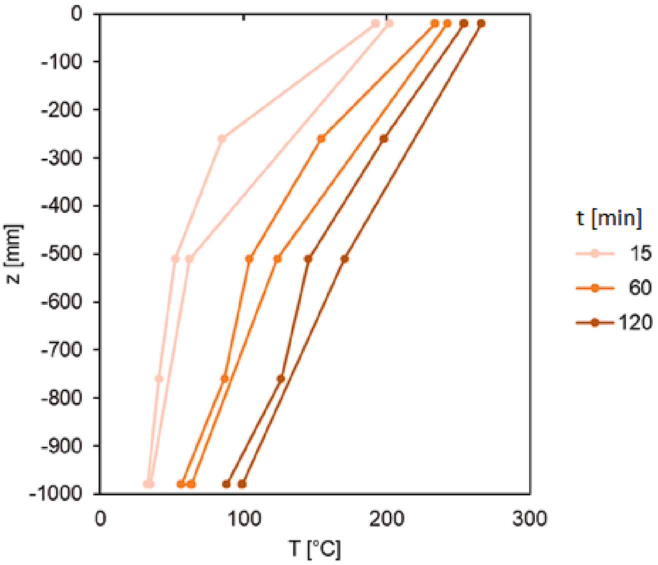

Fig. 11. Evolution of the temperature profile along the heat exchange obtained for the test performed at $2kW_e$r.

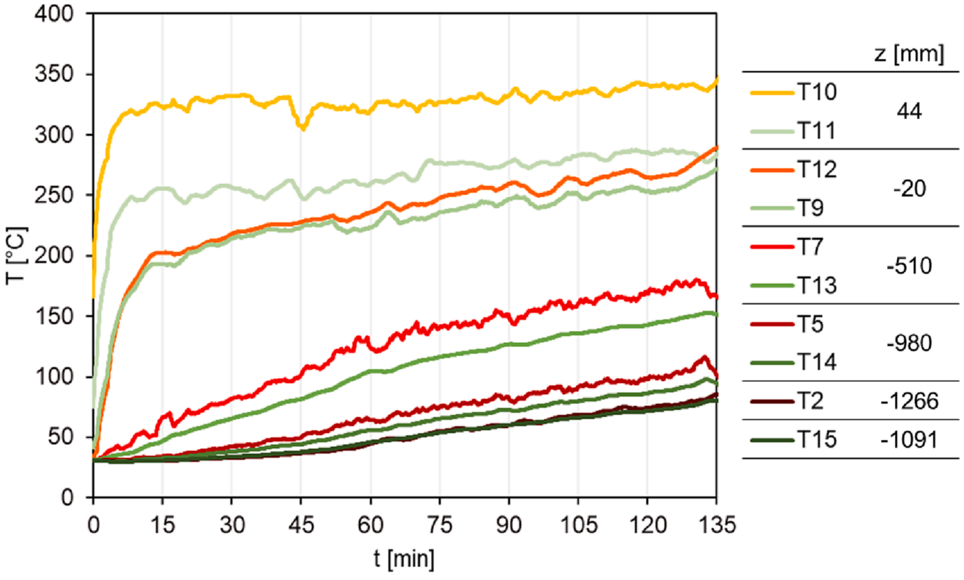

Fig. 10. Time-resolved temperature profiles obtained for the test performed at $2kW_e$.

to be U = 338 W/(m^2 K) in reasonable agreement with the expectations [62].

It is noteworthy that, with the increase of the bottom temperature (T_{r0}), the velocity ratio between the outlet and inlet section of the riser becomes smaller, widening the operative range. For the design value of T_{r0} (about 900 K), the velocity ratio would be $u_{rf}/u_{r0} = 1.33$. So, in the successive experiments at higher input power of the solar simulator, the reservoir heaters were used to boost the increase of T_{r0}. After a while, the heaters were switched off to let the temperatures settle and assess the performance of the heat exchanger with pure irradiation. Fig. 12 shows steady temperature profiles obtained for three different lamp powers. By increasing the irradiation power, the slope of the temperature profiles increases, indicating an increasing efficiency of the heat exchanger.

The same data analysis is repeated (Eqs. (1)–(6)), and the results are gathered in Table 2. It is noteworthy that the standard deviations of ΔT_a and ΔT_{ex}, obtained for different experimental runs carried out with the same operating conditions were about 13 K and 1.0 K respectively. The heat transfer coefficient appears to increase at higher input powers, whereas the heat recovery factor *R* remains close to 90%. These results clearly confirm that autothermal operation of the reactor is feasible.

3.4.2. *Operation under reactive conditions*

The two calcination experiments performed to test the operability of the DIFBAR prototype as a solar reactor were performed consecutively with the same bed inventory. During the first test, a global conversion degree of nearly 10% was obtained. In order to increase the conversion degree, the residence time of the particles inside the receiver was increased during the second experiment, by tuning the control algorithm of the annulus bed level so as to fill the receiver up to a certain height. Taking the riser outlet as a reference height, a volume of about 50 cm^3 could be filled, corresponding to a residence time of the order of 1 min. The results of the second test are reported in Fig. 13, that shows the time evolution of the CO_2 produced and of the global conversion degree (X_g). A conversion of about 50% was reached in 2.5 h, after the first two hours required for the reactor heating. When operating the reactor with this strategy, an average calcination rate of 5.7 mmol/min was obtained between 180 and 260 min, peaking at 30 mmol/min, corresponding to local conversion degrees (X_f) respectively of 12 and 69%.

Focusing on shorter time intervals it is observed that, during the operation of the reactor, the calcination rate strongly fluctuates due to oscillations of the bed level. Fig. 14 shows a strong perturbation of the CO_2 concentration and temperatures signals after a relatively stable period. The temperature in the receiver is quite stable at about 750 °C, until the bed level in the annulus is raised up to the riser outlet, causing a drop in the thermocouple signal between 193 and 197 min. Correspondingly, the residence time of the particles in the receiver increases, driving to a relevant increase in the calcination rate, evidenced by the peak of CO_2 concentration at 15%. The calcination rate $\dot{n}$ ranges from an average value of 4.8 mmol/min between 180 and 190 min (X_f = 7.4%) up to an average value of 22 mmol/min between 194 and 197 min (X_f = 34%).

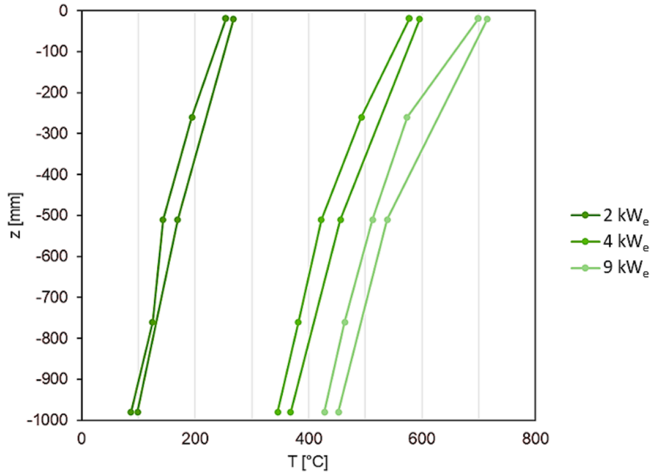

Fig. 12. Temperature profiles along the heat exchanger for different lamp powers.

Table 2
Results of the thermal characterization for different lamp powers.

Lamp power [kW$_e$]	ΔT_a [K]	ΔT_{ex} [K]	*R* -	U [W/(m^2 K)]
2	169	18.5	90%	338
4	228	27.0	89%	366
9	263	29.8	89%	396

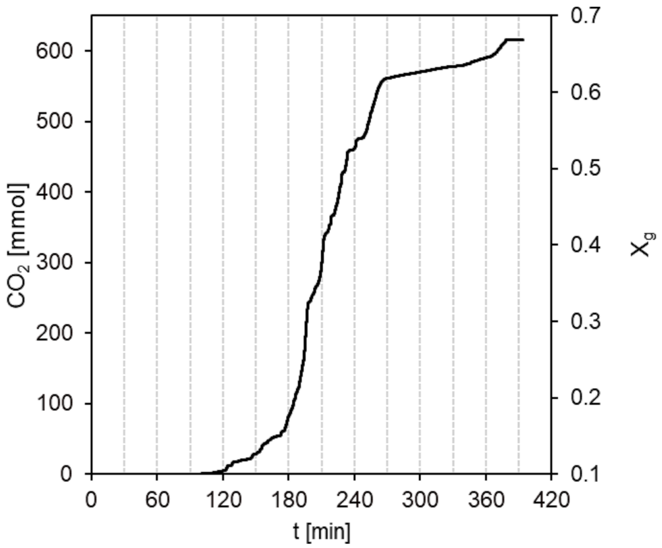

Fig. 13. Cumulative CO_2 production and global conversion degree during the calcination test.

Fig. 15 shows the temperature profile averaged on the time interval between 180 and 190 min. The heat recovery factor is calculated as *R* = 89%, in agreement with the values of the inert tests, and only slightly reduced by the reaction term. The heat transfer coefficient results U = 488 W/(m^2 K). It is noteworthy that the temperatures are slightly lower than those of the inert experiments with sand, even if the power of the solar simulator is the same. The cause is probably the deposition on the window of fine particles generated from calcination, that reduced the transmissivity through the aperture.

Altogether, the results of the reactive tests proved that the DIFBAR can be efficiently employed as chemical reactor for carrying out solar-driven gas–solid chemical processes. The effective sensible heat recovery of the products stream allowed a significant decrease in the solar input required for the course of chemical reactions, which opens the path towards higher overall process efficiencies.

4. Conclusions

A laboratory prototype of the DIFBAR has been built, set-up and operated. The “Single tank” scheme has been tested, in which the solid continuously circulates between the receiver and a reservoir, but different schemes might be studied in the future thanks to the modular design. The system features a circulation loop composed by a fluidized bed riser, the conical cavity receiver, an overflow standpipe (the annulus) and the reservoir. Hydrodynamic control is fundamental for the operation of the reactor. Cold flow experiments with a Geldart B sand have proved the efficacy of the adopted control systems and

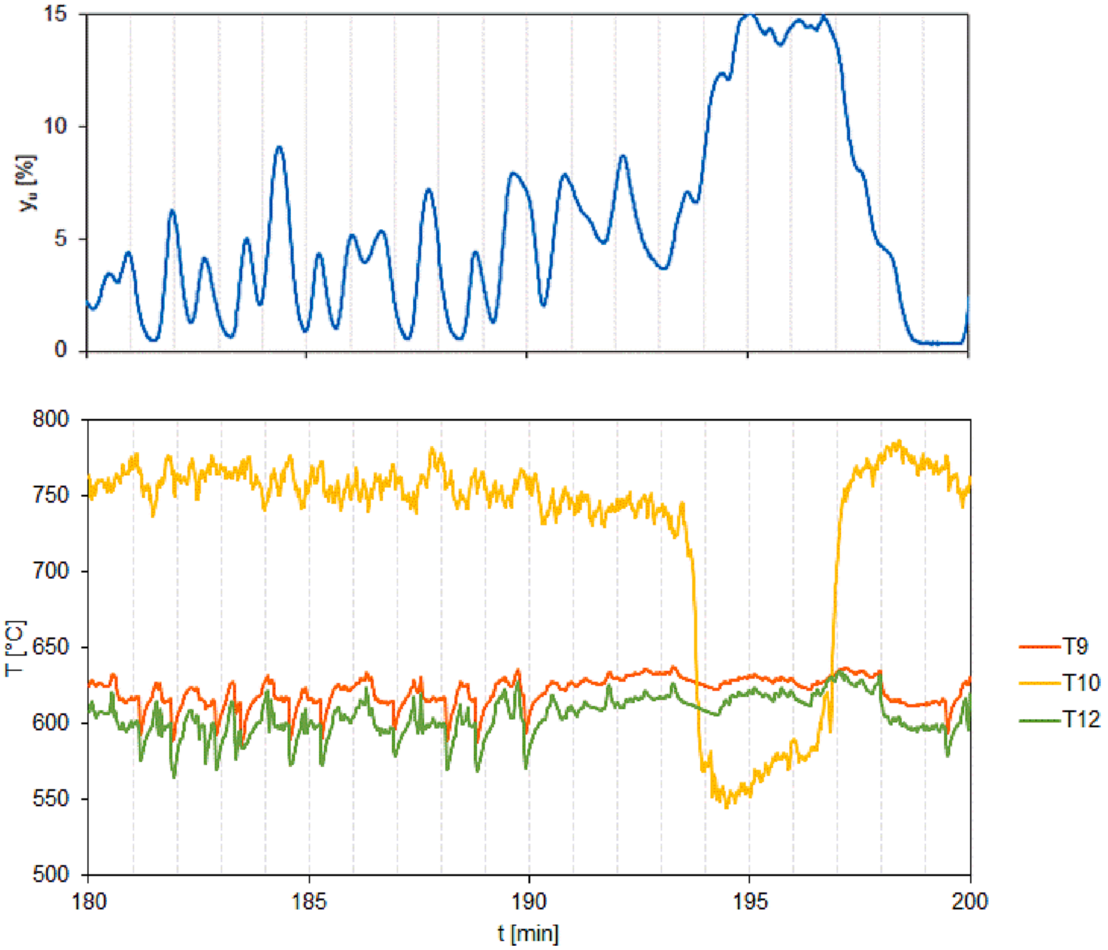

Fig. 14. CO_2 concentration (up) and temperatures (down) time-resolved profiles during $MgCO_3$ calcination.

highlighted the effect of operative variables on the solid flowrates and gas by-passing flowrates, that can be summarized as follows:

- The solid circulation flowrate W can be regulated with the riser gas velocity u_1 and set to the target value of 1.4 g/s, required for the operation of the heat exchanger.
- The auxiliary gas stream Q_3 properly controls the discharge flowrate from the annulus with the mechanism of an L-valve and ensures steady circulation.
- Pressure measurements can be used to adequately monitor and control the annulus bed level, which is fundamental for the effective heat transfer to the riser.
- The reservoir can be operated as a moving or fluidized bed according to process needs. When the reservoir is not aerated ($u_2 = 0$), the solid circulation flowrate W shows an upper limit of about 2 g s^{-1}. This limit disappears when the reservoir is aerated, and its bottom pressure (P6) is increased either by increasing the gas velocity (u_2) or by increasing the outlet pressure drop (P4).
- Calculations indicate that the gas by-passing flowrates through the two standpipes connections are very small (less than 2% of the riser feed). In addition, gas tracing tests have shown evidence that by-passing flows can be reversed and therefore reduced to zero by tuning the operating conditions.

These results provide useful knowledge to understand the principles underlying the hydrodynamic control of the system and to improve its design.

The prototype was then insulated and heated with an in-house built high-flux solar simulator for high temperature experiments with the same inert sand. The heat transfer coefficient of the heat exchanger was calculated from temperature profiles and ranges between 340 and 490 W/(m^2 K), in agreement with previous results. A heat recovery factor of 90% has been calculated, demonstrating clearly that autothermal operation of the reactor is feasible.

Reactive tests were performed, mixing $MgCO_3$ particles to the sand inventory. Results showed that, to obtain a significant calcination rate, it was necessary to increase the residence time of the particles inside the receiver to about 1 min, by increasing the bed level up to about the riser outlet. With this strategy, an average calcination rate of 5.7 mmol/min with a peak value of 30 mmol/min, corresponding to local conversion degrees (X_f) of 12 and 69%, respectively, was obtained. A conversion of about 50% was reached in 2.5 h. These preliminary reaction tests provide a first demonstration of the working principle of the DIFBAR, and the results obtained lay the groundwork for future studies aiming at the optimization of the reactor design and testing new solar processes.

Role of funding source

The study has received financial support by the Ministry of Education, University and Research (MIUR) – Italy, in the frame of the project PON 2015-2020: “ARS01_00985 BIOFEEDSTOCK – Development of Integrated Technological Platforms for Residual Biomass Exploitation”.

CRediT authorship contribution statement

Stefano Padula: Conceptualization, Formal analysis, Investigation, Methodology, Visualization, Writing – original draft. **Maurizio Troiano:** Conceptualization, Methodology, Writing – review & editing.

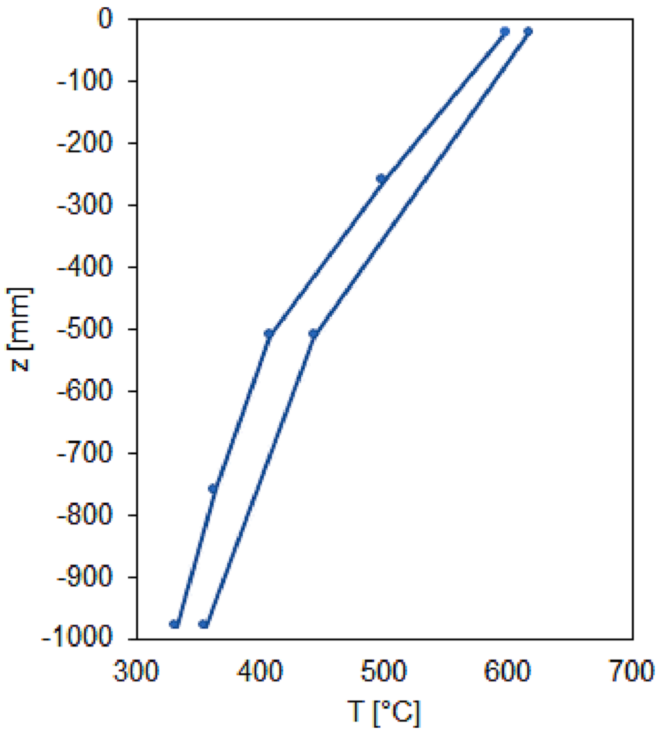

Fig. 15. Temperature profile along the heat exchanger during stable operation of $MgCO_3$ calcination.

Claudio Tregambi: Conceptualization, Methodology, Writing – review & editing. **Roberto Solimene:** Conceptualization, Methodology, Supervision, Writing – review & editing. **Piero Salatino:** Conceptualization, Methodology, Supervision, Writing – review & editing.

Declaration of Competing Interest

The authors declare that they have no known competing financial interests or personal relationships that could have appeared to influence the work reported in this paper.

Data availability

Data will be made available on request.

Acknowledgments

The authors gratefully acknowledge Mr Antonio Cammarota for the set-up of the experimental apparatus, and Tammaro Bencivenga, Antonio Cante, and Ernesto Marinò for the set-up of the ancillary equipment.

References

[1] Gil A, Medrano M, Martorell I, Lázaro A, Dolado P, Zalba B, et al. State of the art on high temperature thermal energy storage for power generation. Part 1 — Concepts, materials and modellization. Renew Sustain Energy Rev 2010;14(1):31–55.

[2] Valero A, Valero A, Calvo G, Ortego A. Material bottlenecks in the future development of green technologies. Renew Sustain Energy Rev 2018;93:178–200. https://doi.org/10.1016/j.rser.2018.05.041.

[3] Medrano M, Gil A, Martorell I, Potau X, Cabeza LF. State of the art on high-temperature thermal energy storage for power generation. Part 2 — Case studies. Renew Sustain Energy Rev 2010;14:56–72. https://doi.org/10.1016/j.rser.2009.07.036.

[4] Zhang H, Baeyens J, Cáceres G, Degrève J, Lv Y. Thermal energy storage: Recent developments and practical aspects. Prog Energy Combust Sci 2016;53:1–40. https://doi.org/10.1016/j.pecs.2015.10.003.

[5] Nie F, Bai F, Wang Z, Li X, Yang R. Solid particle solar receivers in the next-generation concentrated solar power plant. EcoMat 2022:1–27. https://doi.org/10.1002/eom2.12207.

[6] Yadav D, Banerjee R. A review of solar thermochemical processes. Renew Sustain Energy Rev 2016;54:497–532. https://doi.org/10.1016/j.rser.2015.10.026.

[7] André L, Abanades S, Flamant G. Screening of thermochemical systems based on solid-gas reversible reactions for high temperature solar thermal energy storage. Renew Sustain Energy Rev 2016;64:703–15. https://doi.org/10.1016/j.rser.2016.06.043.

[8] Castilla GM, Guío-Pérez DC, Papadokonstantakis S, Johnsson F, Pallarès D. Techno-economic assessment of calcium looping for thermochemical energy storage with CO2 capture. Energies 2021;14:1–17. https://doi.org/10.3390/en14113211.

[9] Edwards SEB, Materić V. Calcium looping in solar power generation plants. Sol Energy 2012;86:2494–503. https://doi.org/10.1016/j.solener.2012.05.019.

[10] Di Lauro F, Tregambi C, Montagnaro F, Salatino P, Chirone R, Solimene R. Improving the performance of calcium looping for solar thermochemical energy storage and CO2 capture. Fuel 2021;298:120791. https://doi.org/10.1016/j.fuel.2021.120791.

[11] André L, Abanades S. Evaluation and performances comparison of calcium, strontium and barium carbonates during calcination/carbonation reactions for solar thermochemical energy storage. J Storage Mater 2017;13:193–205. https://doi.org/10.1016/j.est.2017.07.014.

[12] Agrafiotis C, Roeb M, Sattler C. A review on solar thermal syngas production via redox pair-based water/carbon dioxide splitting thermochemical cycles. Renew Sustain Energy Rev 2015;42:254–85. https://doi.org/10.1016/j.rser.2014.09.039.

[13] Krenzke PT, Fosheim JR, Davidson JH. Solar fuels via chemical-looping reforming. Sol Energy 2017;156:48–72. https://doi.org/10.1016/j.solener.2017.05.095.

[14] Roeb M, Neises M, Monnerie N, Call F, Simon H, Sattler C, et al. Materials-Related Aspects of Thermochemical Water and Carbon Dioxide Splitting: A Review. Materials 2012;5(11):2015–54.

[15] Scheffe JR, Steinfeld A. Oxygen exchange materials for solar thermochemical splitting of H2O and CO2: A review. Mater Today 2014;17:341–8. https://doi.org/10.1016/j.mattod.2014.04.025.

[16] Alxneit I. Assessing the feasibility of separating a stoichiometric mixture of zinc vapor and oxygen by a fast quench - Model calculations. Sol Energy 2008;82:959–64. https://doi.org/10.1016/j.solener.2008.05.009.

[17] Nakamura T. Hydrdogen production from water utilizing solar heat at high temperatures. Sol Energy 1977;19:467–75. https://doi.org/10.1016/0038-092X(77)90102-5.

[18] Ehrensberger K, Frei A, Kuhn P, Oswald HR, Hug P. Comparative experimental investigations of the water-splitting reaction with iron oxide Fe1-yO and iron manganese oxides (Fe1-xMnx)1-yO. Solid State Ion 1995;78:151–60. https://doi.org/10.1016/0167-2738(95)00019-3.

[19] Muhich CL, Ehrhart BD, Witte VA, Miller SL, Coker EN, Musgrave CB, et al. Predicting the solar thermochemical water splitting ability and reaction mechanism of metal oxides: A case study of the hercynite family of water splitting cycles. Energ Environ Sci 2015;8(12):3687–99.

[20] Evdou A, Zaspalis V, Nalbandian L. La1-xSrxFeO3-δ perovskites as redox materials for application in a membrane reactor for simultaneous production of pure hydrogen and synthesis gas. Fuel 2010;89:1265–73. https://doi.org/10.1016/j.fuel.2009.09.028.

[21] Scheffe JR, Steinfeld A. Thermodynamic analysis of cerium-based oxides for solar thermochemical fuel production. Energy Fuel 2012;26:1928–36. https://doi.org/10.1021/ef201875v.

[22] Luciani G, Landi G, Aronne A, Di Benedetto A. Partial substitution of B cation in La0.6Sr0.4MnO3 perovskites: A promising strategy to improve the redox properties useful for solar thermochemical water and carbon dioxide splitting. Sol Energy 2018;171:1–7. https://doi.org/10.1016/j.solener.2018.06.058.

[23] Padula S, Tregambi C, Troiano M, Di Benedetto A, Salatino P, Landi G, et al. Chemical Looping Reforming with Perovskite-Based Catalysts for Thermochemical Energy Storage. Energies (Basel) 2022;15(22):8556.

[24] Puig-Arnavat M, Tora EA, Bruno JC, Coronas A. State of the art on reactor designs for solar gasification of carbonaceous feedstock. Sol Energy 2013;97:67–84. https://doi.org/10.1016/j.solener.2013.08.001.

[25] Lapp J, Davidson JH, Lipi W. Efficiency of two-step solar thermochemical non-stoichiometric redox cycles with heat recovery. Energy 2012;37:591–600. https://doi.org/10.1016/j.energy.2011.10.045.

[26] Steinfeld A, Sanders S, Palumbo R. Design aspects of solar thermochemical engineering—a case study: two-step water-splitting cycle using the Fe3O4/FeO redox system. Sol Energy 1999;65(1):43–53.

[27] Zsembinszki G., Sole A., Barreneche C., Prieto C., Fernández A.I., Cabeza L.F. Review of reactors with potential use in thermochemical energy storage in concentrated solar power plants. Energies 2018;11,2358. doi:10.3390/en11092358.

[28] Alonso E, Romero M. Review of experimental investigation on directly irradiated particles solar reactors. Renew Sustain Energy Rev 2015;41:53–67. https://doi.org/10.1016/j.rser.2014.08.027.

[29] Osinga T, Frommherz U, Steinfeld A, Wieckert C. Experimental investigation of the solar carbothermic reduction of ZnO using a two-cavity solar reactor. J Solar Energy Eng Trans ASME 2004;126:633–7. https://doi.org/10.1115/1.1639001.

[30] Piatkowski N, Wieckert C, Steinfeld A. Experimental investigation of a packed-bed solar reactor for the steam-gasification of carbonaceous feedstocks. Fuel Process Technol 2009;90:360–6. https://doi.org/10.1016/j.fuproc.2008.10.007.

[31] Wieckert C, Frommherz U, Kräupl S, Guillot E, Olalde G, Epstein M, et al. A 300 kW Solar chemical pilot plant for the carbothermic production of zinc. J Solar Energy Eng Trans ASME 2007;129:190–6. https://doi.org/10.1115/1.2711471.

[32] Flamant G, Hernandez D, Bonet C, Traverse J-P. Experimental aspects of the thermochemical conversion of solar energy; Decarbonation of CaCO3. Sol Energy 1980;24:385–95. https://doi.org/10.1016/0038-092X(80)90301-1.

[33] Tescari S, Neumann NC, Sundarraj P, Moumin G, Rincon Duarte JP, Linder M, et al. Storing solar energy in continuously moving redox particles – Experimental analysis of charging and discharging reactors. Appl Energy 2022;308:118271. https://doi.org/10.1016/j.apenergy.2021.118271.

[34] Haueter P, Moeller S, Palumbo R, Steinfeld A. The production of zinc by thermal dissociation of zinc oxide - Solar chemical reactor design. Sol Energy 1999;67:161–7. https://doi.org/10.1016/s0038-092x(00)00037-2.

[35] Schunk LO, Haeberling P, Wept S, Wuillemin D, Meier A, Steinfeld A. A receiver-reactor for the solar thermal dissociation of zinc oxide. J Solar Energy Eng Trans ASME 2008;130:0210091–6. https://doi.org/10.1115/1.2840576.

[36] Koepf E, Villasmil W, Meier A. Pilot-scale solar reactor operation and characterization for fuel production via the Zn/ZnO thermochemical cycle. Appl Energy 2016;165:1004–23. https://doi.org/10.1016/j.apenergy.2015.12.106.

[37] Martin J, Vitko JJ. ASCUAS: a solar central receiver utilizing a solid thermal carrier; 1982. Doi:10.2172/5663779.

[38] Ho CK, Christian J, Yellowhair J, Jeter S, Golob M, Nguyen C, et al. Highlights of the high-temperature falling particle receiver project: 2012–2016. AIP Conf Proc 2017;1850:2012–6. https://doi.org/10.1063/1.4984370.

[39] Tan T, Chen Y. Review of study on solid particle solar receivers. Renew Sustain Energy Rev 2010;14:265–76. https://doi.org/10.1016/j.rser.2009.05.012.

[40] Steinfeld A, Brack M, Meier A, Weidenkaff A, Wuillemin D. A solar chemical reactor for co-production of zinc and synthesis gas. Energy 1998;23:803–14. https://doi.org/10.1016/S0360-5442(98)00026-7.

[41] Chinnici A, Arjomandi M, Tian ZF, Lu Z, Nathan GJ. A Novel Solar Expanding-Vortex Particle Reactor: Influence of Vortex Structure on Particle Residence Times and Trajectories. Sol Energy 2015;122:58–75. https://doi.org/10.1016/j.solener.2015.08.017.

[42] Davis D, Troiano M, Chinnici A, Saw WL, Lau T, Solimene R, et al. Particle residence time distributions in a vortex-based solar particle receiver-reactor: An experimental, numerical and theoretical study. Chem Eng Sci 2020;214:115421. https://doi.org/10.1016/j.ces.2019.115421.

[43] Flamant G. Theoretical and experimental study of radiant heat transfer in a solar fluidized-bed receiver. AIChE J 1982;28:529–35. https://doi.org/10.1002/aic.690280402.

[44] Tregambi C, Troiano M, Montagnaro F, Solimene R, Salatino P. Fluidized Beds for Concentrated Solar Thermal Technologies—A Review. Front Energy Res 2021;9:1–26. https://doi.org/10.3389/fenrg.2021.618421.

[45] Jiang K, Du X, Zhang Q, Kong Y, Xu C, Ju X. Review on gas-solid fluidized bed particle solar receivers applied in concentrated solar applications: Materials, configurations and methodologies. Renew Sustain Energy Rev 2021;150:111479. https://doi.org/10.1016/j.rser.2021.111479.

[46] Tregambi C, Chirone R, Montagnaro F, Salatino P, Solimene R. Heat transfer in directly irradiated fluidized beds. Sol Energy 2016;129:85–100. https://doi.org/10.1016/j.solener.2016.01.057.

[47] Salatino P, Ammendola P, Bareschino P, Chirone R, Solimene R. Improving the thermal performance of fluidized beds for concentrated solar power and thermal energy storage. Powder Technol 2016;290:97–101. https://doi.org/10.1016/j.powtec.2015.07.036.

[48] Migliozzi S, Paulillo A, Chirone R, Salatino P, Solimene R. Hydrodynamics of compartmented fluidized beds under uneven fluidization conditions. Powder Technol 2017;316:476–91. https://doi.org/10.1016/j.powtec.2016.12.052.

[49] Gokon N, Mataga T, Kondo N, Kodama T. Thermochemical two-step water splitting by internally circulating fluidized bed of NiFe2O4 particles: Successive reaction of thermal-reduction and water-decomposition steps. Int J Hydrogen Energy 2011;36:4757–67. https://doi.org/10.1016/j.ijhydene.2011.01.076.

[50] Gokon N, Kumaki S, Miyaguchi Y, Bellan S, Kodama T, Cho H. Development of a 5kWth internally circulating fluidized bed reactor containing quartz sand for continuously-fed coal-coke gasification and a beam-down solar concentrating system. Energy 2019;166:1–16. https://doi.org/10.1016/j.energy.2018.10.036.

[51] Chuayboon S, Abanades S, Rodat S. Insights into the influence of biomass feedstock type, particle size and feeding rate on thermochemical performances of a continuous solar gasification reactor. Renew Energy 2019;130:360–70. https://doi.org/10.1016/j.renene.2018.06.065.

[52] Solimene R, Chirone R, Chirone R, Salatino P. Dynamic modeling of a solar receiver/thermal energy storage system based on a compartmented dense gas fluidized bed. AIP Conference Proceedings 2017;1850,080026. 10.1063/1.4984447.

[53] STEM®-CST Concentrated Solar Thermal n.d. https://www.magaldigreenenergy.com/en/stem.

[54] Hoskins AL, Millican SL, Czernik CE, Alshankiti I, Netter JC, Wendelin TJ, et al. Continuous on-sun solar thermochemical hydrogen production via an isothermal redox cycle. Appl Energy 2019;249:368–76. https://doi.org/10.1016/j.apenergy.2019.04.169.

[55] Zhang H, Benoit H, Perez-Lopèz I, Flamant G, Tan T, Baeyens J. High-efficiency solar power towers using particle suspensions as heat carrier in the receiver and in the thermal energy storage. Renew Energy 2017;111:438–46. https://doi.org/10.1016/j.renene.2017.03.101.

[56] Miller DC, Pfutzner CJ, Jackson GS. Heat transfer in counterflow fluidized bed of oxide particles for thermal energy storage. Int J Heat Mass Transf 2018;126:730–45. https://doi.org/10.1016/j.ijheatmasstransfer.2018.05.165.

[57] next - CSP http://next-csp.eu/.

[58] Kong W, Wang B, Baeyens J, Li S, Ke H, Tan T, et al. Solids mixing in a shallow cross-flow bubbling fluidized bed. Chem Eng Sci 2018;187:213–22. https://doi.org/10.1016/j.ces.2018.04.073.

[59] Esence T, Benoit H, Poncin D, Tessonneaud M, Flamant G. A shallow cross-flow fluidized-bed solar reactor for continuous calcination processes. Sol Energy 2020;196:389–98. https://doi.org/10.1016/j.solener.2019.12.029.

[60] Ermanoski I, Siegel NP, Stechel EB. A New Reactor Concept for Efficient Solar-Thermochemical Fuel Production. J Sol Energy Eng 2013;135:1–10. https://doi.org/10.1115/1.4023356.

[61] Falter CP, Pitz-paal R. Modeling counter-flow particle heat exchangers for two-step solar thermochemical syngas production. Appl Therm Eng 2018;132:613–23. https://doi.org/10.1016/j.applthermaleng.2017.12.087.

[62] Tregambi C, Bevilacqua C, Troiano M, Solimene R, Salatino P. A novel autothermal fluidized bed reactor for concentrated solar thermal applications. Chem Eng J 2020;398:125702. https://doi.org/10.1016/j.cej.2020.125702.

[63] Tregambi C, Padula S, Galbusieri M, Coppola G, Montagnaro F, Salatino P, et al. Directly irradiated fluidized bed reactor for thermochemical energy storage and solar fuels production. Powder Technol 2020;366:460–9. https://doi.org/10.1016/j.powtec.2020.02.045.

[64] Padula S., Tregambi C., Solimene R., Chirone R., Troiano M., Salatino P. A novel fluidized bed “ thermochemical battery ” for energy storage in concentrated solar thermal technologies. Energy Convers Manag 2021;236,113994. doi:10.1016/j.enconman.2021.113994.

[65] Perry RH. Perry’s Chemical Engineer’s Handbook. 8th ed. McGraw Hill Education; 2008.